Simple assessment for rotation of the forearm using three-dimensional bone models

van Loon, Derek F.R.; Siemensma, Mark F.; van Es, Eline M.; Eygendaal, Denise; Veeger, H.E.J.; Colaris, Joost W.

Simple assessment for rotation of the forearm using three-dimensional bone models

Derek F.R. van Loon [a,*], Mark F. Siemensma [a], Eline M. van Es [a], Denise Eygendaal [a], DirkJan H.E.J. Veeger [b], Joost W. Colaris [a]

[a] Department of Orthopaedics and Sports Medicine, Erasmus MC, University Medical Center Rotterdam, Dr. Molewaterplein 40, Rotterdam 3015 GD, the Netherlands
[b] Department of Biomechanical Engineering, Delft University of Technology, Mekelweg 2, Delft 2628 CD, the Netherlands

ABSTRACT

Background: Dynamic medical imaging can determine the cause of rotational impairment in the forearm. However, it has drawbacks depending on the image modality used, related to radiation dose, the need for specialized equipment, and the labor intensity involved in the analysis. Because the forearm rotation axis is static, we hypothesize that an axis based on bony landmarks is comparable to an axis calculated from dynamic imaging.
Methods: Eight post-mortem human forearms were scanned using CT in seven rotational positions from maximum supination to maximum pronation. Three rotation axes were calculated: the landmark, average helical, and circle fit axes. The primary outcome is the difference between the axes expressed as the angle and the minimal distance between them. Secondary outcomes are the orientation errors when modeling pose using the three found axes.
Findings: The mean difference between the landmark and average helical axes was 0.38 degrees and 0.51 mm. The mean difference between the landmark and circle fit axes was 0.40 degrees and 0.51 mm. When modeling the pose of the radius using one of the three axes, the difference between the modeled radius and the scanned radius was in each direction below 2 mm and 1 degree.
Interpretation: The rotation axis of the forearm can be accurately calculated using automatically placed bony landmarks. These findings indicate that determining the forearm rotation axis does not require multiple static images or dynamic imaging. This knowledge should be applied to clinical data to assess its applicability in practice.

1. Introduction

Forearm fractures are among the most common fractures in children and adults (Andreasen et al., 2023; Körner et al., 2020). The primary treatment involves closed or open fracture reduction, accompanied by the application of either a cast, intramedullary nails, or plate osteosynthesis to stabilize the realigned forearm bones (Caruso et al., 2021; Truntzer et al., 2015). This treatment aims to restore the original shape. One complication that occurs if the original shape is not appropriately restored is called a malunion: the union of a bone in an abnormal shape (Serra Lopez et al., 2023). The incidence of radiographic forearm malunions varies widely in the literature, ranging from 19 to 35 % in patients up to 15 years of age (Cognet and Mares, 2021; Katt et al., 2020; Li et al., 2022). The primary symptom of a forearm malunion is rotational impairment. However, not all patients with a radiographic malunion experience a clinically relevant loss of function (Colaris et al., 2014).

To evaluate the role of the bones in impaired forearm rotation at a patient-specific level, the in vivo movement of the radius and ulna must be visualized. Multiple imaging modalities can be used for dynamic medical imaging, such as computed tomography (CT), radiography, or magnetic resonance imaging (MRI). Dynamic CT visualizes the bones in three dimensions (3D) in relatively high resolution, but the limited field-of-view (FOV) and high radiation dosages are disadvantages of this technique (Choi et al., 2013; Iordache et al., 2017). Dynamic fluoroscopy with one or two x-ray sources lowers the radiation dose but only visualizes movement in 2D (Akhbari et al., 2021; Matsuki et al., 2010). Dynamic MRI requires no radiation and can visualize bones in 3D. However, it also suffers from a limited FOV, requires specific magnetic coils and patient setup, and has a lower image quality than CT (Garetier et al., 2020). Furthermore, all the images acquired from these modalities

---

* Corresponding author.
E-mail address: d.vanloon@erasmusmc.nl (D.F.R. van Loon).

require a lot of post-processing before any information can be visualized and retrieved (Blum et al., 2020).

A more straightforward solution would be modeling movement from a static CT scan based on two landmarks. This solution is viable because the forearm rotation axis is determined by two pivot joints, the proximal and distal radioulnar joints, separated by the long diaphyses of the radius and ulna. These joints both have one degree of freedom and would thus together form a hinge joint. This is confirmed by multiple studies, which have shown that the rotation axis of the forearm is static and runs from the proximal radial head to the ulnar fovea (Matsuki et al., 2010; Oonk et al., 2023; Veeger et al., 1997). This new axis must be compared to a kinematically derived axis from multiple CT scans to justify the simplification.

Therefore, our study aims to compare the landmark axis (LMA) retrieved from one CT scan to the average helical axis (AHA) and circle fit axis (CFA), both derived from multiple CT scans. We hypothesize that the LMA differs by less than one degree and one millimeter from AHA and CFA.

2. Methods

2.1. Image acquisition and processing

The arms of eight postmortem human subjects (PMHS) (aged 61–90, seven female, seven right arms) were scanned with the forearm in seven different rotational positions using a fixating setup using a Siemens NAEOTOM Alpha CT scanner (Siemens Healthineers AG, Erlangen, Germany). The CT protocol we used is described previously (Booij et al., 2023).

Each arm was fixated into a custom setup (see Fig. 1). The humerus was fixated to a vertical plate with the elbow in 90° flexion. The wrist was fixated using Velcro and two wedges with 30°/60° angles. Using the wedges, the forearm was positioned in steps of 30° from 90° supination to 90° pronation by placing the wedges underneath the wrist. If the wrist could not reach 90° pronation or supination, the maximum rotation without over-exertion was used. No wedges were used for maximal pronation or supination. The neutral position, defined as the position of the wrist in which the thumb points towards the shoulder, was acquired by placing the two wedges with 90° sides on both sides of the wrist (see Fig. 2). The definition of the neutral position follows section 4, part 2 of the recommendation of the International Society of Biomechanics (ISB) for Joint Coordinate Systems (JSC) (Wu et al., 2005).

In every position the radius and ulna were segmented using Materialise Mimics Version 25.0 (Materialise NV, Liege, Belgium), and 3D bone surface models were retrieved as STL files. The 3D models of the left forearm were mirrored to be identical to the right forearm. Anatomical landmarks were automatically placed on the 3D bone surface models using a validated algorithm, which had median differences of 2 mm between the automatically and manually placed landmarks (van Loon et al., 2024). The forearm in the neutral position (the fourth

position in Fig. 1) is the reference position. The ulnae of the measured positions were transformed to ulna in the reference pose; see Fig. 3A. Registration consisted of an initial alignment of the landmarks followed by an iterative closest point (ICP) registration, explained in Appendix A.2.1.

The seven poses of the radius were calculated relative to the reference pose of the ulna using landmarks. Coordinate systems (CS) were equal to the definitions in section 4, part 2 of the recommendation of the ISB, with two exceptions (Wu et al., 2005). First, the *y*-axis of the ulna is determined by landmarks instead of the axis of inertia. Second, the *y*-axis of the radius is based on its entire length rather than only the distal half. The landmarks and CSs are visualized in Appendix A.1. The equations used to calculate the CSs can be found in Appendix A.2.4.

2.2. Rotation axis

To validate the use of a rotation axis derived from landmarks (LMA) on a single static CT scan, two reference axes are calculated from all scanned forearms for comparison. These axes are the average helical axis (AHA) and the circle fit axis (CFA). These axes are visualized in Fig. 3B, C, and D, respectively, and in the animation in the Supplementary material. All equations used to calculate the axes can be found in Appendix A.2.

The direction of the LMA is the vector from the ulnar fovea landmark to the radial head center. The origin of the LMA is the ulnar fovea landmark.

The AHA is calculated by first calculating the finite helical axis (FHA) for each transformation of the radius from one pose to another relative to the ulna (Spoor and Veldpaus, 1980; Woltring, 1990). The FHA is calculated based on the seven CSs of the radius. The AHA is the weighted average of the FHAs, with a more significant weighting for larger rotations (Ehrig and Heller, 2019; Stokdijk et al., 1999).

The CFA is calculated by fitting two three-dimensional circles on two sets of landmarks. A proximal circle is calculated from the radial tuberosity landmarks of all scans. A distal circle is calculated from the radial styloid landmarks of all scans. The CFA is the vector from the distal circle center to the proximal circle center (Oonk et al., 2023; Shiode et al., 2024).

Primary outcomes are the angles and minimum distances between the three axes. The mean and standard deviation of the angle and minimum distance between the axes were calculated. Furthermore, errors of estimates are given for the AHA and CFA. Regarding the AHA, the deviation between the FHAs and the AHA was calculated for each specimen in terms of position and orientation as root mean squared error (RMSE) (Ancillao, 2022; Stokdijk et al., 1999). The mean and standard deviation of the eight RMSEs are presented. Regarding the CFA, the error of estimates is given by the RMSE of all the distances between the fitted circle and the used landmarks (Oonk et al., 2023). All equations used to calculate the errors can be found in Appendix A.2.5 and Appendix A.2.6.
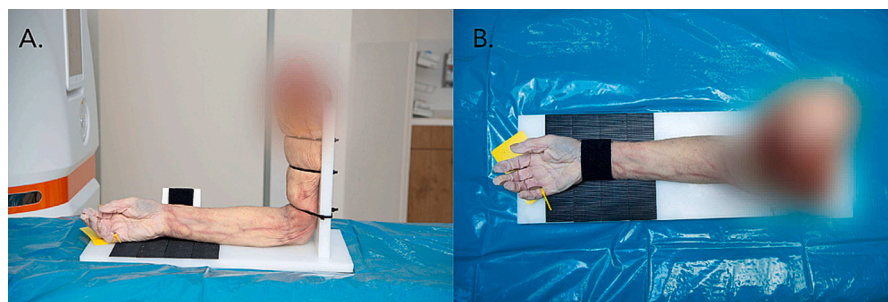

Fig. 1. Photos of the used fixation setup. The forearm was placed on a plate with Velcro underneath the wrist to fixate it. The humerus was fixated with straps to a perpendicular plate to minimize movement. A: lateral side-view of the setup, using one wedge to position the forearm in 30° supination. B: The top view of the setup with the forearm is maximal supination.
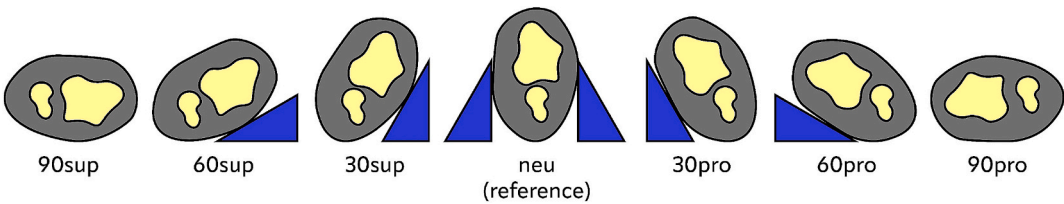
Fig. 2. Schematic drawing of how the wedges were placed to fixate the wrist in a certain rotational position. The wrist was placed in three supination (sup) and three pronation (pro) positions. The wrist in the neutral position (neu) was used as a reference position for the modeling.
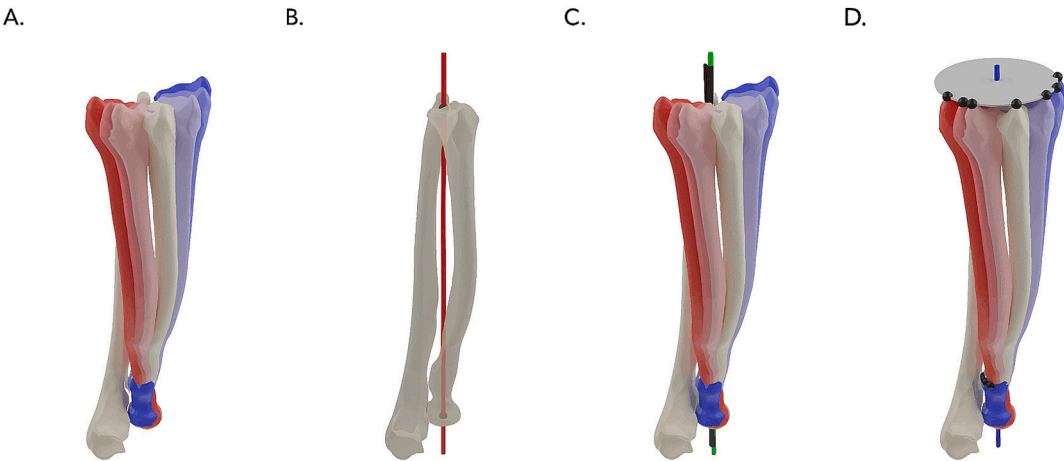

Fig. 3. A: the ulnae of the rotated forearm are aligned with the ulna in the neutral position using surface registration, which shows the rotation of the radius around the ulna. B: the landmark axis (LMA) is drawn as a red line and is the vector from the radial head center to the ulnar fovea. C: the average helical axis (AHA) in green is calculated by averaging all the finite helical axes. D: The circle fit axis (CFA) is drawn in blue and is the vector between the centers of two circles, which fit on the radial styloids and the radial tuberosities of all scanned radii. (For interpretation of the references to colour in this figure legend, the reader is referred to the web version of this article.)

All calculations are done in Python using custom-written code. Parts of the code for determining the FHAs and AHA are based on open-source code written by Ancillao (Ancillao, 2022).

2.3. Pose modeling

To better understand the errors when using a static axis, each of the three axes is used to model the forearm poses. Again, the forearm in the neutral position is used as a reference and, in this case, the starting position. The rotation angle from the neutral position to the six other positions is retrieved using the FHA analysis for each specimen (see Appendix A.2.5). The radius is rotated separately around the LMA, AHA, and CFA, which leads to three modeled radii for each pose.

The difference between the pose of the scanned radius and each modeled pose is calculated. Pose difference is expressed as a translational and rotational error in three directions relative to the coordinate system of the ulna. The rotation matrix is converted into Euler angles in the order *yzx* (pronation, flexion, ulnar deviation) for the rotational errors, following the recommendation of the ISB for the hand and wrist (Wu et al., 2005). All equations used for the pose modeling and retrieving translational and rotational errors can be found in Appendix A.2.8. The mean and standard deviation of the translational and rotational errors in each direction for each pose for each axis are given. Significant differences in translation or rotation errors between the three axes at each pose are calculated using one-way ANOVA. By using the Bonferroni correction to correct for multiple testing, the alpha level is set to $0.05/36 = 0.00139$.

3. Results

3.1. Rotation axis

The difference between the LMA and AHA is 0.38° (SD: 0.34°) and 0.51 (SD: 0.21) millimeters (Table 1). The difference between the LMA and CFA is 0.40° (SD: 0.32°) and 0.51 (SD: 0.31) millimeters (Table 1).

The RMSE of the AHA errors of estimates were 1.44 (SD: 0.53) millimeters and 0.69° (SD: 0.42°). For the CFA, the RMSE of the proximal circle was 0.16 (SD: 0.12) millimeters. The RMSE of the distal circle was 0.15 (SD: 0.07) millimeters.

3.2. Pose modeling

The translational pose errors are below one millimeter in the axial direction in every used axis (range − 0.27–0.20 mm) (Fig. 4A). The error in the sagittal direction (range − 1.66–1.16 mm) do not exceed 2 mm (Fig. 4C). This is also true for the coronal direction (range − 1.23–1.02 mm), but significant errors between the used axes are found in the poses of 60° and 90° supination (Fig. 4E). Using the LMA or CFA, the radius translates more to the volar direction. In contrast, using the AHA, the radius translated dorsally compared to the scanned radius. The mean

Table 1
Mean and standard deviation angular and distance difference between axes. AHA: average helical axis; CFA: circle fit axis; LMA: landmark axis.

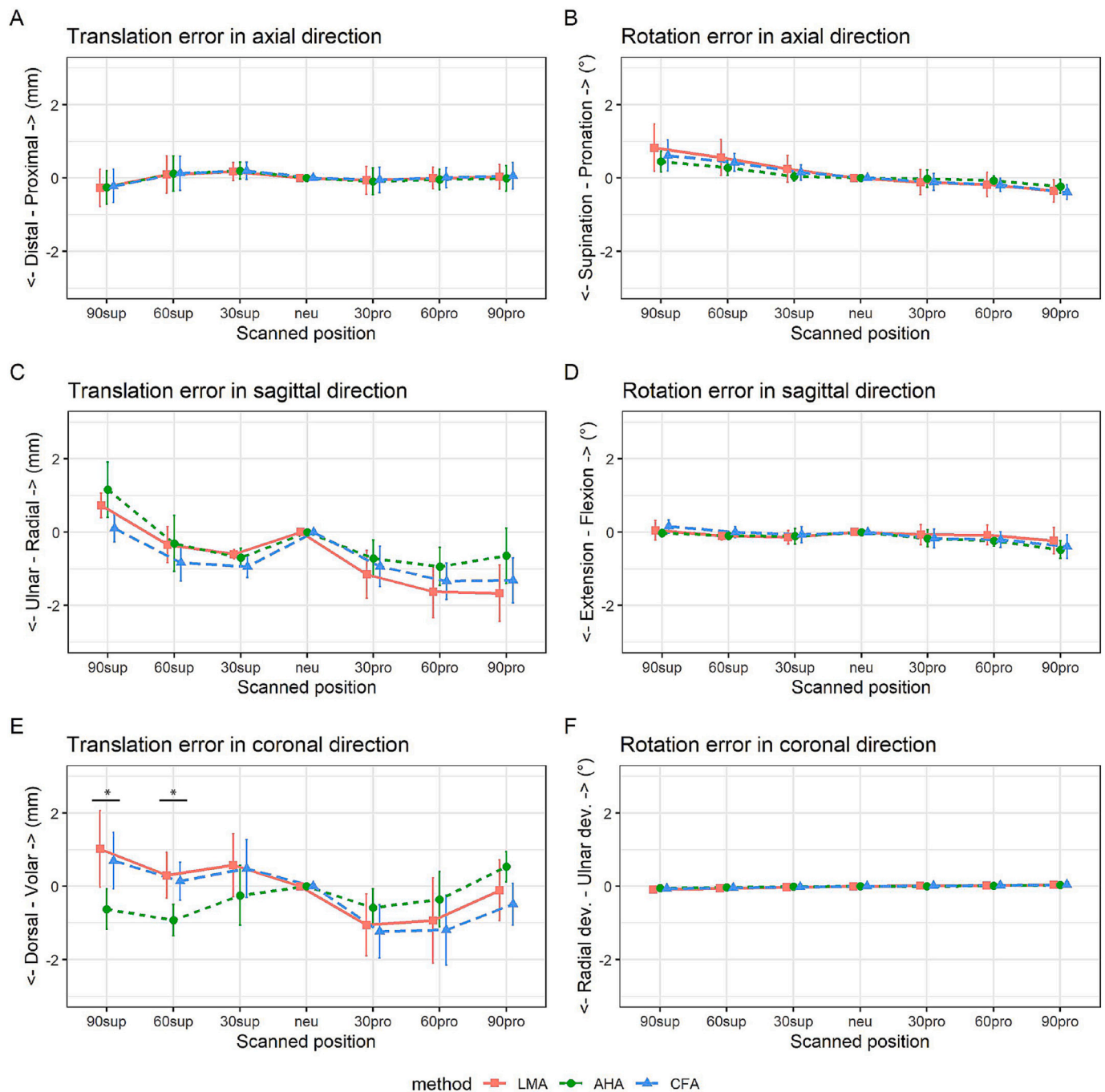|	Angle (°)	Distance (mm)
LMA ↔ AHA	0.38 (0.34)	0.51 (0.21)
LMA ↔ CFA	0.40 (0.32)	0.51 (0.31)
AHA ↔ CFA	0.27 (0.14)	0.91 (0.62)

Fig. 4. Orientation errors when modeling the pose of the radius using one of the three axes. Error bars indicate standard deviation, and asterisks indicate significance below 0.00139. A: translational error in the axial plane; B: rotational error in the axial plane; C: translational error in the sagittal plane; D: rotational error in the sagittal plane; E: translational error in the coronal plane; F: rotational error in the coronal plane. LMA: landmark axis; AHA: average helical axis; CFA: circle fit axis; dev: deviation.

rotational errors in the axial (range − 0.39–0.82), sagittal (range − 0.48–0.15), and coronal (range − 0.08–0.05) directions are all below one degree (Fig. 4B, D, E). Rotating the radius around one of the three axes does not result in a significant difference in orientation of the radius.

As a typical example, the modeling of one specimen is shown in Fig. 5. The pose modeling differences of this specimen were the most similar to the found mean errors. The images are stills from an animation showing the pose modeling using the three axes. This animation is provided in the Supplementary Material.

4. Discussion

This study used bony landmarks to recreate the forearm rotation axis automatically and compared this axis with two axes retrieved from multiple scans in different rotation positions. The LMA differed by less than one degree and one millimeter from the AHA and CFA. Thus, the difference between the LMA and the kinematically determined axes is negligibly small. Determining the forearm rotation axis does not require multiple static images or dynamic imaging.

Most of the studies on forearm kinematics focus on retrieving the rotational axis, not on making this knowledge applicable to individual

Fig. 5. Static images from an animation in the Supplementary Material visualizing the modeled radius pose using the three axes for one specimen. In red, the landmark axis is used; in green, the average helical axis; in blue, the circle fit axis. A: modeling the maximum pronation; B: modeling the maximum supination. (For interpretation of the references to colour in this figure legend, the reader is referred to the web version of this article.)

anatomy. Almost all research on retrieving the rotation axis has shown that the radius rotates around a static axis (Baeyens et al., 2006; Nakamura et al., 1999; Oonk et al., 2023; Veeger et al., 1997; Youm et al., 1979). These studies report minor errors of estimates of the AHA, which aligns with our findings. Two more recent articles used a circle-fitting approach to estimate the rotation axis (Oonk et al., 2023; Shiode et al., 2021), and one showed that this method is comparable to calculating the AHA (Oonk et al., 2023). For this method, the errors of estimates were minimal as well.

Because the angular and distance differences between the axes only give precise results on whether or not the axes are alike, the message can be abstract for clinicians. Therefore, we added pose modeling as a secondary result. Fig. 5 and the animations in the Supplementary material show deviations from the found static axes when modeling rotation. While the modeled radius differs from the scanned radius in every pose, the differences are negligible, independent of the used axis. Most translation differences are less than one millimeter, and all differences are below two millimeters. The rotational differences are below one degree. Only a significant difference between the axes in volar translation can be found when modeling extreme poses of supination.

This study also has some limitations. First, we have excluded the humerus and focused only on the radius's rotation relative to the ulna. Thus, the ulnar motion relative to the humerus during forearm rotation is not considered. We have excluded the humerus from the analysis to ensure that the knowledge and LMA remain applicable even when the humerus is unavailable. Moreover, multiple studies have shown that the movement of the ulna is minimal (Akhbari et al., 2021; Baeyens et al., 2006; Tay et al., 2010). Second, the choice of cadaveric specimens in combination with multiple static CT scans instead of healthy volunteers and dynamic imaging is based on ethical considerations regarding the radiation exposure. A disadvantage of using cadaveric specimens is that the age is often higher than in studies using healthy volunteers, and the variability of forearm function during life is unknown. To capture forearm rotation as naturally as possible, we choose not to mimic rotation using an internal fixator but only use wedges. Our results of the found average helical axis are comparable to other image-based studies (Matsuki et al., 2010; Nakamura et al., 1999; Oonk et al., 2023; Tay et al., 2010). Third, this study determined the rotation axis in healthy specimens. A malunion could alter kinematics, meaning that the AHA of a malunited forearm is not equal to the LMA. For distal radius malunions, research indicates that kinematics change insignificantly, but joint contact areas and ligament lengths do change. (Crisco et al., 2007; Moore et al., 2002). It is not known if a diaphyseal malunion alters forearm kinematics, but it is known that the distance between the bones is altered, leading to functional limitations (Abe et al., 2018). In both

cases, modeling with the true rotation axis of the patient is not necessarily needed to measure ligament length or the distance between the bones accurately enough to determine the reason for limited rotation after a malunited fracture. Our study shows that a landmark-based axis can accurately reference normal kinematics, which is validated and can be reliably and automatically located. The clinical applicability now needs to be researched using patient data.

5. Conclusion

We have shown that forearm rotation can be simulated based on automatically placed bony landmarks on patient-specific 3D bone models. The landmark axis is comparable to the average helical or circle fit axes. To assess the clinical applicability of this knowledge, the model could be used on 3D models from patients with a rotational impairment of the forearm to see if the predicted rotation matches the measured function and to find the underlying reason for function loss.

Supplementary data to this article can be found online at https://doi.org/10.1016/j.clinbiomech.2025.106590.

CRediT authorship contribution statement

Derek F.R. van Loon: Writing – original draft, Visualization, Validation, Methodology, Formal analysis, Conceptualization. **Mark F. Siemensma:** Writing – review & editing, Writing – original draft. **Eline M. van Es:** Writing – review & editing, Resources, Methodology, Conceptualization. **Denise Eygendaal:** Writing – review & editing, Supervision. **DirkJan H.E.J. Veeger:** Writing – review & editing, Supervision, Conceptualization. **Joost W. Colaris:** Writing – review & editing, Supervision, Resources, Conceptualization.

Declaration of competing interest

The authors declare that they have no known competing financial interests or personal relationships that could have appeared to influence

Appendices

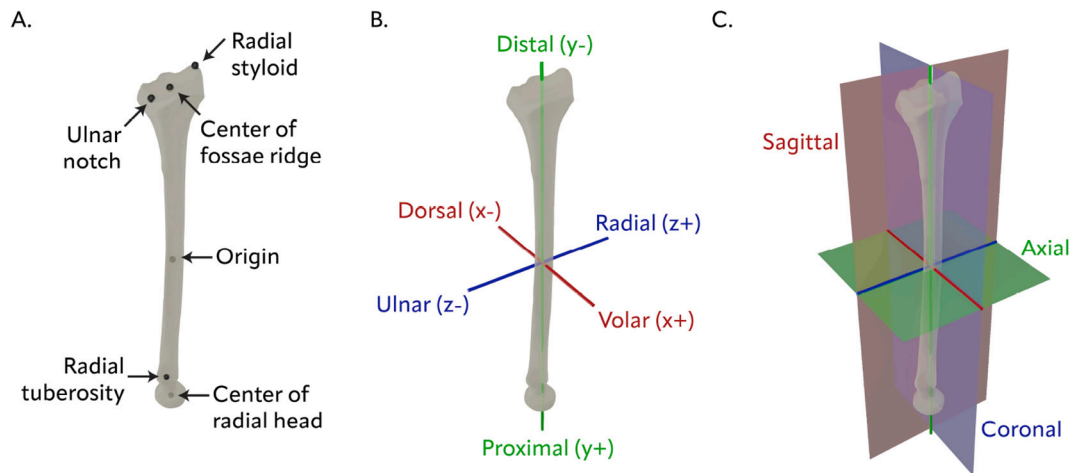*A.1. Landmarks and coordinate systems*

Fig. A.6. Coordinate system of the right radius. A: landmarks of the radius; B: directions of the coordinate system of the radius; C: planes of the coordinate system of the radius.
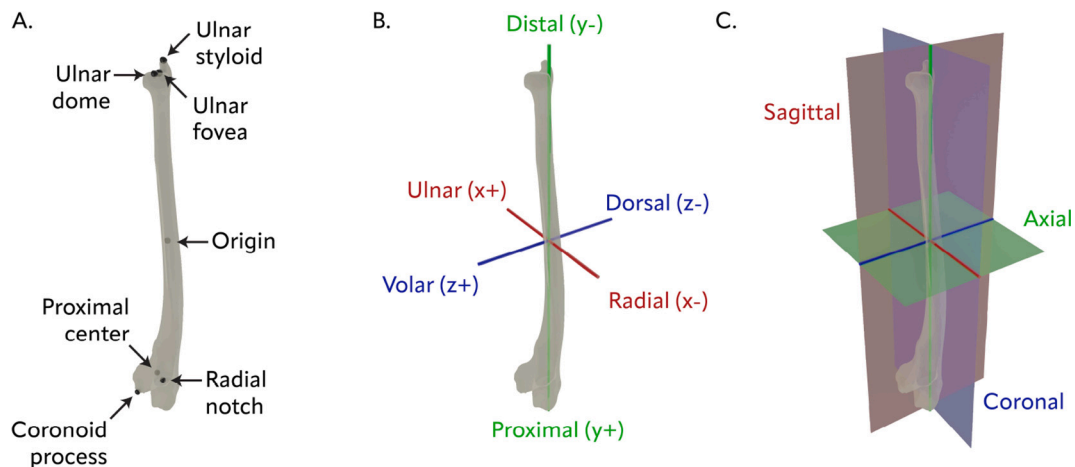
Fig. A.7. Coordinate system of the right ulna. A: landmarks of the ulna; B: directions of the coordinate system of the ulna; C: planes of the coordinate system of the ulna.

A.2. Equations

A.2.1. Aligning 3D surface models (Procrustes analysis and iterative closest point algorithm)

In our study, the forearm was scanned in seven positions. The bone surface model of the ulna in every position was aligned with the ulna in the neutral position, the fourth position of the seven. The radii are moved along. This transformation is calculated by performing a registration between the surfaces. The registration between two surfaces is done by performing a Procrustes analysis and an iterative closest point (ICP) algorithm to refine the alignment. The ICP algorithm is sensitive to local minima, which can be avoided by first calculating a rough alignment on a few landmarks. The Procrustes analysis finds the transformation matrix, which describes the mapping of a set of moving 3D points $\mathbf{P}_i$ to another set of fixed 3D points $\mathbf{P}_j$. In our case, the 3D points are the landmarks of the bones. No scaling or reflecting of the meshes and their landmarks is allowed. First, the translation is calculated using the mean of both sets of landmarks $\mathbf{P}_{i,center}$ and $\mathbf{P}_{j,center}$ and subtracted from each landmark.

$$\mathbf{P}_{i,center} = \frac{1}{N}\sum_{k=1}^{N}\mathbf{P}_k$$

$$\mathbf{P}_{j,center} = \frac{1}{N}\sum_{k=1}^{N}\mathbf{P}_k$$

(A.1)

Here, N equals the number of landmarks. The centered landmarks for the moving surface $\mathbf{P}'_i$ and the fixed surface $\mathbf{P}'_j$ are then calculated.

$$\mathbf{P}'_i = \mathbf{P}_i - \mathbf{P}_{i,center}$$
$$\mathbf{P}'_j = \mathbf{P}_j - \mathbf{P}_{j,center}$$

(A.2)

Then, the cross-covariance matrix M is calculated using the centered landmarks. The optimal rotation matrix R is calculated using singular value decomposition.

$$\mathbf{M} = \mathbf{P}'^T_j\mathbf{P}'_i$$

$$\mathbf{M} = \mathbf{U\Sigma V^T}$$

$$\mathbf{R} = \mathbf{U}\begin{bmatrix} 1 & 0 & 0 \\ 0 & 1 & 0 \\ 0 & 0 & \det(\mathbf{UV^T}) \end{bmatrix}\mathbf{V}^T$$

(A.3)

In here, U and V are the orthogonal matrices and Σ is a diagonal matrix with singular values. With the rotation matrix R the translation component t can be computed.

$$\mathbf{t} = \mathbf{P}_{j,center} - \mathbf{RP}_{i,center}$$

(A.4)

Together, they form an initial transformation matrix $\mathbf{T}_{init}$.

$$\mathbf{T}_{init} = \begin{pmatrix} R_{1,1} & R_{1,2} & R_{1,3} & t_1 \\ R_{2,1} & R_{2,2} & R_{2,3} & t_2 \\ R_{3,1} & R_{3,2} & R_{3,3} & t_2 \\ 0 & 0 & 0 & 1 \end{pmatrix}$$

(A.5)

This initial transformation is refined using an iterative closest point (ICP) algorithm. This algorithm aims to minimize the distance between the vertices of the moving 3D model $\mathbf{V}_i$ and the surface of the fixed 3D model $\mathbf{s}_j$. First, the initial transformation is applied to $\mathbf{V}_i$, which results in the transformed vertices $\mathbf{V}'_i$

$$\mathbf{V}'_i = \mathbf{T}_{init}\cdot\mathbf{V}_i$$

(A.6)

For each vertex in $\mathbf{V}'_i$, a point $\mathbf{s}_{closest,i}$ with the shortest distance to the surface of the fixed model s_j is calculated.

$$\mathbf{s}_{closest,i} = \underset{\mathbf{s}_j}{\operatorname{argmin}}\|\mathbf{V}'_i - \mathbf{s}_j\|$$

(A.7)

Then, a new transformation matrix $\mathbf{T}_{new}$ is calculated, which aligns $\mathbf{V}'_i$ to $\mathbf{s}_{closest,i}$. This is done using a Procrustes analysis, as explained above. This transformation is applied to the centered vertices $\mathbf{V}'_i$ to obtain a new aligned set of vertices $\mathbf{V}''_i$. The total transformation $\mathbf{T}_{total}$, consisting of only the initial transformation at first, is updated.

$$\mathbf{V}''_i = \mathbf{T}_{new}\cdot\mathbf{V}'_i$$

(A.8)

$$\mathbf{T}_{total} = \mathbf{T}_{new}\cdot\mathbf{T}_{total}$$

(A.9)

This process is repeated until the change in cost $|C_k - C_{k-1}|$, describing how well the transformation improves between two iterations, is (1) below a certain threshold, or (2) the maximum number of iterations $k = K$ is reached. This study's threshold was $1\cdot10^{-5}$, and the maximum number of iterations was 20.

$$C_k = \frac{1}{N}\sum_{i=1}^{n}\left\|\mathbf{V}''_i - \mathbf{s}_{closest,i}\right\|^2$$

(A.10)

$$|C_k - C_{k-1}| < \text{threshold}$$

(A.11)

A.2.2. Landmark axis

The landmark axis (LMA) is defined by a location $\mathbf{S}_{LMA}$ and direction $\mathbf{n}_{LMA}$, which can be directly calculated from two landmarks taken from the forearm in neutral forearm rotation: the radial head center $\mathbf{P}_{RH,4}$ and ulnar fovea $\mathbf{P}_{UF,4}$.

$$\mathbf{S}_{LMA} = \mathbf{P}_{UF,4}$$

(A.12)

$$\mathbf{n}_{LMA} = \frac{\left(\mathbf{P}_{RH,4} - \mathbf{P}_{UF,4}\right)}{\left\|\mathbf{P}_{RH,4} - \mathbf{P}_{UF,4}\right\|}$$

(A.13)

A.2.3. Plane fitting algorithm

To fit a plane through a set of at least three points, the points $\mathbf{P}_N$ are first centered with the mean $\mathbf{C}_{plane}$, resulting in $\mathbf{P}'_i$. Then, their covariance matrix is calculated.

$$\mathbf{C}_{plane} = \frac{1}{N} \sum_{i=1}^{N} \mathbf{P}_i \text{ for } i \text{ in } \mathbf{P}_N \tag{A.14}$$

$$\mathbf{P}'_i = \mathbf{P}_i - \mathbf{C}_{plane} \tag{A.15}$$

$$\mathbf{M} = \mathbf{P}'^{T}_i \mathbf{P}'_i \tag{A.16}$$

Using singular value decomposition (see Eq. A.3), the plane normal $\mathbf{n}_{plane}$ is calculated by normalizing the third column of the left singular matrix U.

$$\mathbf{n}_{plane} = U[\ldots, 3] \tag{A.17}$$

A.2.4. Coordinate systems

The radius coordinate system $\mathbf{CS}_{rad}$ is equal to the International Society of Biomechanics (ISB) recommendation for joint coordinate systems (JCS) of the hand and wrist, with one exception. The y-axis is based on the entire length of the radius rather than only the distal half. The origin $\mathbf{O}_{rad}$ of $\mathbf{CS}_{rad}$ lies at the center of the radius bone halfway between the radial head center $\mathbf{P}_{RH}$ and the center of the fossae ridge $\mathbf{P}_{FR}$. The location at which an intersection of the 3D model and a plane is made can be found with

$$\mathbf{O}_{rad} = 0.5(\|\mathbf{P}_{RH} - \mathbf{P}_{FR}\|) \frac{\mathbf{P}_{RH} - \mathbf{P}_{FR}}{\|\mathbf{P}_{RH} - \mathbf{P}_{FR}\|} + \mathbf{P}_{RH} \tag{A.18}$$

and the normal of this plane is equal to the y-axis $\mathbf{Y}_{rad}$.

$$\mathbf{Y}_{rad} = \frac{\mathbf{P}_{RH} - \mathbf{P}_{FR}}{\|\mathbf{P}_{RH} - \mathbf{P}_{FR}\|} \tag{A.19}$$

A temporary z-axis $\mathbf{Z}_{rad,temp}$ lies in a plane through three points: the radial styloid $\mathbf{P}_{RS}$, the ulnar notch $\mathbf{P}_{UN}$, and the found origin $\mathbf{O}_{rad}$. The normal of the plane $\mathbf{n}_{plane}$ is calculated with the plane fitting algorithm explained earlier. Using $\mathbf{n}_{plane}$ and $\mathbf{Y}_{rad}$ the z-axis $\mathbf{Z}_{rad,temp}$ is calculated with

$$\mathbf{Z}_{rad,temp} = \frac{\mathbf{n}_{plane} \times \mathbf{Y}_{rad}}{\|\mathbf{n}_{plane} \times \mathbf{Y}_{rad}\|} \tag{A.20}$$

The x-axis $\mathbf{X}_{rad}$ is the common line perpendicular to $\mathbf{Y}_{rad}$ and $\mathbf{Z}_{rad,temp}$.

$$\mathbf{X}_{rad} = \frac{\mathbf{Y}_{rad} \times \mathbf{Z}_{rad,temp}}{\|\mathbf{Y}_{rad} \times \mathbf{Z}_{rad,temp}\|} \tag{A.21}$$

At last, the perpendicular z-axis $\mathbf{Z}_{rad}$ can be calculated similarly.

$$\mathbf{Z}_{rad} = \frac{\mathbf{Y}_{rad} \times \mathbf{X}_{rad}}{\|\mathbf{Y}_{rad} \times \mathbf{X}_{rad}\|} \tag{A.22}$$

$\mathbf{CS}_{rad}$ can be constructed.

$$\mathbf{CS}_{rad} = \begin{bmatrix} X_{rad,1} & Y_{rad,1} & Z_{rad,1} & O_{rad,1} \\ X_{rad,2} & Y_{rad,2} & Z_{rad,2} & O_{rad,2} \\ X_{rad,3} & Y_{rad,3} & Z_{rad,3} & O_{rad,3} \\ 0 & 0 & 0 & 1 \end{bmatrix} \tag{A.23}$$

In this study, the ulna coordinate system $\mathbf{CS}_{uln}$ is based on the same section of the ISB recommendation as the radius. The origin of the ulnar coordinate system $\mathbf{O}_{uln}$ lies at the center of the bone halfway between the proximal center $\mathbf{P}_{PC}$ and the ulnar dome $\mathbf{P}_{UD}$. The location at which an intersection of the 3D model and a plane is made can be found with

$$\mathbf{O}_{uln} = 0.5(\|\mathbf{P}_{PC} - \mathbf{P}_{UD}\|) \frac{\mathbf{P}_{PC} - \mathbf{P}_{UD}}{\|\mathbf{P}_{PC} - \mathbf{P}_{UD}\|} + \mathbf{P}_{PC} \tag{A.24}$$

and the normal of this plane is equal to the y-axis.

$$\mathbf{Y}_{uln} = \frac{\mathbf{P}_{PC} - \mathbf{P}_{UD}}{\|\mathbf{P}_{PC} - \mathbf{P}_{UD}\|} \tag{A.25}$$

A temporary ulnar x-axis $\mathbf{X}_{Uln,temp}$ equals the radial x-axis in the neutral forearm rotation $\mathbf{X}_{rad,4}$. Of the seven scanned forearm poses, the neutral position is the fourth.

$$\mathbf{X}_{uln,temp} = \mathbf{X}_{rad,4} \tag{A.26}$$

The z-axis is the cross-product of the y-axis and the x-axis and must also be normalized.

$$\mathbf{Z}_{uln} = \frac{\mathbf{Y}_{uln} \times \mathbf{X}_{uln,temp}}{\|\mathbf{Y}_{uln} \times \mathbf{X}_{uln,temp}\|} \tag{A.27}$$

At last, the perpendicular x-axis $\mathbf{X}_{uln}$ can be calculated similarly.

$$\mathbf{X}_{uln} = \frac{\mathbf{Y}_{uln} \times \mathbf{Z}_{uln}}{\|\mathbf{Y}_{uln} \times \mathbf{Z}_{uln}\|} \tag{A.28}$$

$\mathbf{CS}_{uln}$ can be constructed.

$$\mathbf{CS}_{uln} = \begin{bmatrix} X_{uln,1} & Y_{uln,1} & Z_{uln,1} & O_{uln,1} \\ X_{uln,2} & Y_{uln,2} & Z_{uln,2} & O_{uln,2} \\ X_{uln,3} & Y_{uln,3} & Z_{uln,3} & O_{uln,3} \\ 0 & 0 & 0 & 1 \end{bmatrix} \tag{A.29}$$

A.2.5. Finite helical axis and average helical axis

To determine the average helical axis (AHA), the average orientation and position of all transformations of one radial pose to another are calculated. Calculating the AHA benefits from expressing all CSs relative to one consistent CS of the moving object. This expression simplifies the calculation of their relative motion. In our case, the CSs of the ulnae $\mathbf{CS}_{uln,N}$ and radii $\mathbf{CS}_{rad,N}$ are expressed relative to the radius in the neutral position $\mathbf{CS}_{rad,4}$.

$$\begin{aligned} \mathbf{CS}_{rad,i \to rad,4} &= \left(\mathbf{CS}_{rad,4}\right)^{-1} \cdot \mathbf{CS}_{rad,i} \\ \mathbf{CS}_{uln,i \to rad,4} &= \left(\mathbf{CS}_{rad,4}\right)^{-1} \cdot \mathbf{CS}_{uln,i} \end{aligned} \tag{A.30}$$

Then, the motion of the radius is expressed relative to the ulna in the neutral position.

$$\mathbf{CS}_{rad,i \to uln,4} = \left(\mathbf{CS}_{uln,4 \to rad,4}\right)^{-1} \cdot \mathbf{CS}_{rad,i \to rad,1} \tag{A.31}$$

The transformation between two poses i and j of the radius $\mathbf{T}_{rad,i \to rad,j}$ can then be calculated.

$$\mathbf{T}_{rad,i \to rad,j} = \left(\mathbf{CS}_{rad,i \to uln}\right)^{-1} \cdot \mathbf{CS}_{rad,j \to uln} \text{ for } i \text{ in } N, j = i + 1 \tag{A.32}$$

The transformations between the same positions and transformations in the opposite direction are not calculated. The total amount of transformations k is

$$k = \sum_{i=1}^{N} (N - i) \tag{A.33}$$

in which N is the total number of scanned positions. Given a transformation matrix $\mathbf{T}_i$, the rotation matrix $\mathbf{R}$ and translation vector $\mathbf{O}$ can be found.

$$\begin{aligned} \mathbf{T}_i &= \begin{pmatrix} \ddots & \vdots & \iddots & \vdots \\ \cdots & \mathbf{R} & \cdots & \mathbf{O} \\ \iddots & \vdots & \ddots & \vdots \\ 0 & 0 & 0 & 1 \end{pmatrix} \\ &= \begin{pmatrix} R_{1,1} & R_{1,2} & R_{1,3} & O_1 \\ R_{2,1} & R_{2,2} & R_{2,3} & O_2 \\ R_{3,1} & R_{3,2} & R_{3,3} & O_2 \\ 0 & 0 & 0 & 1 \end{pmatrix} \text{ for } i \text{ in } k \end{aligned} \tag{A.34}$$

Given $\mathbf{R}$, the rotation angle ϕ can be calculated.

$$\sin(\phi) = \frac{1}{2} \sqrt{\left(R_{3,2} - R_{2,3}\right)^2 + \left(R_{1,3} - R_{3,1}\right)^2 + \left(R_{2,1} - R_{1,2}\right)^2}$$

$$\cos(\phi) = \frac{1}{2}\left(R_{1,1} + R_{2,2} + R3, 3 - 1\right)$$

$$\phi = \begin{cases} \arcsin\ (\sin(\phi)\,|\sin(\phi)\,) \le \dfrac{\sqrt{2}}{2} \\ \arccos\ (\cos(\phi)\,|\sin(\phi)\,) > \dfrac{\sqrt{2}}{2} \end{cases} \tag{A.35}$$

Given the rotation angle, the direction $\mathbf{n}_{FHA}$ and position $\mathbf{S}_{FHA}$ of the finite helical axis can be calculated.

$$\mathbf{n}_{FHA} = \frac{1}{2\sin(\phi)} \begin{bmatrix} R_{3,2} - R_{2,3} \\ R_{1,3} - R_{3,1} \\ R_{2,1} - R_{1,2} \end{bmatrix}^T \tag{A.36}$$

$$\mathbf{S}_{FHA} = \left(-\frac{1}{2}\mathbf{n}_{FHA}\right) \times (\mathbf{n}_{FHA} \times \mathbf{O}) + \left(\left(\frac{\sin(\phi)}{2(1 - \cos(\phi))}\mathbf{n}_{FHA}\right) \times \mathbf{O}\right) \tag{A.37}$$

All found $\mathbf{n}_{FHA}$ and $\mathbf{S}_{FHA}$ are called $\mathbf{n}_N$ and $\mathbf{S}_N$. The optimal direction $\mathbf{n}_{AHA}$ and optimal pivot point $\mathbf{S}_{FHA}$ can be found by the following equations.

$$\mathbf{n}_{AHA} = \sum_{i=1}^{k} w_i \left(\mathbf{n}_i \mathbf{n}_i^T \right) \tag{A.38}$$

$$\mathbf{S}_{AHA} = \left(\frac{1}{k} \sum_{i=1}^{k} w_i \left(\mathbf{I} - \mathbf{n}_i \mathbf{n}_i^T \right) \right)^{-1} \left(\frac{1}{k} \sum_{i=1}^{k} w_i \left(\mathbf{I} - \mathbf{n}_i \mathbf{n}_i^T \right) \mathbf{S}_i \right) \tag{A.39}$$

In the determination of $\mathbf{S}_{AHA}$, a weighing factor w_{ij} is introduced. This factor prioritized rotations with a larger rotation angle by decreasing the influence of noise due to small rotations.

$$w_{ij} = \sin^2 \left(\frac{\phi_{i,j}}{2} \right) \tag{A.40}$$

The AHA estimates error regarding direction E_n and position E_S can be calculated.

$$E_S = \sqrt{\frac{1}{N} \sum_{i=1}^{N} \left(\frac{|(\mathbf{S}_{AHA} - \mathbf{S}_i) \cdot (\mathbf{n}_{AHA} \times \mathbf{n}_i)|}{\|(\mathbf{n}_{AHA} \times \mathbf{n}_i)\|} \right)^2} \tag{A.41}$$

$$E_n = \sqrt{\frac{1}{N} \sum_{i=1}^{N} \left(\cos^{-1} (\mathbf{n}_i \cdot \mathbf{n}_{AHA}) \right)^2} \tag{A.42}$$

A.2.6. Circle fit axis

Given a set of 3D points $\mathbf{P}_{LM,N}$, we want to fit a circle as close as possible to the set of points. The points of this circle can be represented as:

$$\mathbf{P}_{circle}(t) = r\cos(t)\mathbf{u} + r\sin(t)(\mathbf{n} \times \mathbf{u}) + \mathbf{C}, \quad 0 \le t \le 2\pi \tag{A.43}$$

in which r is the radius of the circle, $\mathbf{C}$ is the center, $\mathbf{n}$ is the normal unit vector, $\mathbf{u}$ is a unit vector in any direction perpendicular to $\mathbf{n}$. These vectors can be calculated by specifying the orientation of the circle in space using a zenith angle ϕ and azimuth angle θ.

$$\mathbf{n} = \begin{pmatrix} \cos(\phi)\sin(\theta) \\ \sin(\phi)\sin(\theta) \\ \cos(\theta) \end{pmatrix}, \mathbf{u} = \begin{pmatrix} -\sin(\phi) \\ \cos(\phi) \\ 0 \end{pmatrix} \tag{A.44}$$

To fit a circle in 3D, a plane is fit on a set of points $\mathbf{P}_{LM}$ to obtain the plane normal $\mathbf{n}_{plane}$. The next step is to project the 3D points on the fitted plane with a 2D coordinate system. The rotation matrix can be found using the Rodrigues rotation formula. A rotation matrix $\mathbf{T}_{rot}$ can be found by calculating an axis of rotation $\mathbf{k}$ and angle of rotation θ from the cross product between the found plane normal and a chosen normal of the new, projected coordinates with their own xy coordinate system, which is $(0,0,1)$.

$$\mathbf{T}_{rot} = \mathbf{P}_{LM,N}\cos(\theta) + \left(\mathbf{k} \times \mathbf{P}_{LM,N} \right) \sin(\theta) + \mathbf{k}\langle \mathbf{k}, \mathbf{P}_{LM,N} \rangle (1 - \cos(\theta)) \tag{A.45}$$

$$\mathbf{k} = \mathbf{n}_{plane} \times (0,0,1)^T \tag{A.46}$$

Applying the rotation matrix $\mathbf{T}_{rot}$ to $\mathbf{P}_{LM,N}$ gives a set of 2D coordinates, on which a 2D circle can be fitted. The equation for a 2D circle with radius r and center $(x_c, y_c)^T$ is

$$(x - x_c)^2 + (y - y_c)^2 = r^2 \tag{A.47}$$

which can not be solved because there are more equations than unknowns. By rewriting, we get

$$(2x_c)x + (2y_c)y + \left(r^2 - x_c^2 - y_c^2 \right) = x^2 + y^2 \tag{A.48}$$

$$c_0 x + c_1 y + c_2 = x^2 + y^2 \tag{A.49}$$

in which the unknown parameters r and $(x_c, y_c)^T$ are replaced by $\mathbf{c} = (c_0, c_1, c_2)^T$. Applied to all input points, this leads to a system of linear equations

$$\mathbf{Ac} = \mathbf{b} \tag{A.50}$$

in which

$$\mathbf{A} = \begin{pmatrix} x_0 & y_0 & 1 \\ \vdots & \vdots & \vdots \\ x_{n-1} & y_{n-1} & 1 \end{pmatrix}, \mathbf{b} = \begin{pmatrix} x_0^2 + y_0^2 \\ \vdots \\ x_{n-1}^2 + y_{n-1}^2 \end{pmatrix} \tag{A.51}$$

An approximation can be found using a least-squares algorithm, which minimizes the square sum of residuals $\|\mathbf{b} - \mathbf{Ac}\|^2$.

$$\mathbf{c} = \underset{\mathbf{c} \in \mathbb{R}}{\operatorname{argmin}} \left(\|\mathbf{b} - \mathbf{Ac}\|^2 \right) \tag{A.52}$$

When the circle's center and radius are found, the fit's error of estimates E_{cf} is defined as the root mean squared difference between the distance of each point from P_{LM} to the center and the radius.

$$E_{cf} = \sqrt{\frac{1}{N}\sum_{i=1}^{N}\left(\left\|\mathbf{P}_{LM,i} - \mathbf{C}_{plane}\right\| - r\right)^2} \text{ for } i \text{ in } \mathbf{P}_{LM,N} \tag{A.53}$$

In our case, the algorithm consisting of Eqs. A.43 to A.52 is applied to all the radial styloid landmarks $\mathbf{P}_{RS,N}$ to calculate a distal circle and the radial tuberosity landmarks $\mathbf{P}_{RT,N}$ to calculate a proximal circle.

$$\mathbf{n}_{prox}, \mathbf{C}_{prox}, r_{prox} = \text{circlefit}\left(\mathbf{P}_{RT,N}\right) \tag{A.54}$$

$$\mathbf{n}_{dist}, \mathbf{C}_{dist}, r_{dist} = \text{circlefit}\left(\mathbf{P}_{RS,N}\right) \tag{A.55}$$

The center of the distal circle $\mathbf{C}_{dist}$ gives the position of the circle fit axis $\mathbf{S}_{CFA}$. The direction of the circle fit axis $\mathbf{n}_{CFA}$ is given by the normalized vector pointing from the distal circle's center $\mathbf{C}_{dist}$ to the proximal circle's center $\mathbf{C}_{prox}$.

$$\mathbf{S}_{CFA} = \mathbf{C}_{dist} \tag{A.56}$$

$$\mathbf{n}_{CFA} = \frac{\left(\mathbf{C}_{prox} - \mathbf{C}_{dist}\right)}{\left\|\mathbf{C}_{prox} - \mathbf{C}_{dist}\right\|} \tag{A.57}$$

A.2.7. Angle and distance between axes

The rotation axes in this study are defined by a position vector $\mathbf{S}$ and a normalized direction vector $\mathbf{n}$. By using the LMA and AHA as example, the angle θ between the vectors is given by

$$\theta = \arccos(\mathbf{n}_{LMA} \cdot \mathbf{n}_{AHA}) \tag{A.58}$$

The minimum distance d between the LMA and AHA is given by

$$d = \frac{\left|(\mathbf{S}_{LMA} - \mathbf{S}_{AHA}) \cdot (\mathbf{n}_{LMA} \times \mathbf{n}_{aha})\right|}{\left\|(\mathbf{n}_{LMA} \times \mathbf{n}_{aha})\right\|} \tag{A.59}$$

A.2.8. Pose modeling

The pose of the radius in the neutral position is rotated separately around the LMA, AHA, and CFA. The direction $\mathbf{n}$ and location $\mathbf{S}$ of the axes are already known. The rotation angle ϕ (see Eq. A.35) in radians is found from the FHA analysis. The transformation matrix $\mathbf{T}_{4 \rightarrow i}$ is then

$$c = \cos(\phi_{4 \rightarrow i}) \tag{A.60}$$

$$s = \sin(\phi_{4 \rightarrow i}) \tag{A.61}$$

$$C = 1 - c \tag{A.62}$$

$$\mathbf{R}_{4 \rightarrow i} = \begin{bmatrix} n_1(n_1C) + c & n_1(n_2C) - (n_3c) & n_3(n_1C) + (n_2c) \\ n_1(n_2C) + (n_3c) & n_2(n_2C) + c & n_2(n_3C) - (n_1c) \\ n_3(n_1C) - (n_2c) & n_2(n_3C) + (n_1c) & n_3(n_3C) + c \end{bmatrix} \tag{A.63}$$

$$\mathbf{t}_{4 \rightarrow i} = \mathbf{S} - (\mathbf{R}_{4 \rightarrow i} \cdot \mathbf{S}) \tag{A.64}$$

$$\mathbf{T}_{4 \rightarrow i} = \begin{bmatrix} R_{4 \rightarrow i,1,1} & R_{4 \rightarrow i,1,2} & R_{4 \rightarrow i,1,3} & t_{4 \rightarrow i,1} \\ R_{4 \rightarrow i,2,1} & R_{4 \rightarrow i,2,2} & R_{4 \rightarrow i,2,3} & t_{4 \rightarrow i,2} \\ R_{4 \rightarrow i,3,1} & R_{4 \rightarrow i,3,2} & R_{4 \rightarrow i,3,3} & t_{4 \rightarrow i,3} \\ 0 & 0 & 0 & 1 \end{bmatrix} \tag{A.65}$$

Here, $\mathbf{R}_{4 \rightarrow i}$ is the matrix describing the rotation and $\mathbf{t}_{4 \rightarrow i}$ is the vector describing the translation. First, the transformation must be applied to the pose of the scanned radii. For this example, we use the LMA.

$$\mathbf{CS}_{rad,i}^{LMA} = \mathbf{T}_{4 \rightarrow i}^{LMA} \cdot \mathbf{CS}_{rad,4} \tag{A.66}$$

To retrieve the pose difference between the scanned and modeled radius relative to the ulna, the poses must first be aligned to the radius in the neutral pose and then to the ulna in the neutral pose (see Eq. A.30).

$$\mathbf{CS}_{rad,i \rightarrow rad,4}^{LMA} = \left(\mathbf{CS}_{rad,4}\right)^{-1} \cdot \mathbf{CS}_{rad,i}^{LMA} \tag{A.67}$$

$$\mathbf{CS}_{rad,i \rightarrow uln,4}^{LMA} = \left(\mathbf{CS}_{uln,4 \rightarrow rad,4}\right)^{-1} \cdot \mathbf{CS}_{rad,i \rightarrow rad,4}^{LMA} \tag{A.68}$$

The matrix describing the difference between the modeled pose and the scanned pose of the radius relative to the ulna $\mathbf{D}_{rad,i}^{LMA}$ is then given by

$$\mathbf{D}_{rad,i}^{LMA} = \left(\mathbf{CS}_{rad,i \rightarrow uln,4}\right)^{-1} \cdot \mathbf{CS}_{rad,i \rightarrow uln,4}^{LMA} \tag{A.69}$$

This difference in pose can be expressed as a translational t and a rotational difference R in three directions. The translational difference is the last column of the pose difference matrix.

$$t_{\Delta x} = D_{4,1}$$
$$t_{\Delta y} = D_{4,2}$$
$$t_{\Delta z} = D_{4,3}$$

(A.70)

The rotational difference requires converting the rotational part of the pose difference into Euler angles. This conversion depends on the order of axes and must be defined by the user. The standard order is *yzx*, as defined in section 4.4.2 of part 2 of the ISB recommendation.

$$R_{\Delta x} = \arctan2\ (D_{1,3}, D_{1,1})$$
$$R_{\Delta y} = \arctan2\ \left(-D_{1,2}, \sqrt{(D_{2,2}D_{2,2}) + (D_{3,2}D_{3,2})}\right)$$
$$R_{\Delta z} = \arctan2\ (D_{3,2}, D_{1,1})$$

(A.71)

References

Abe, S., Murase, T., Oka, K., Shigi, A., Tanaka, H., Yoshikawa, H., 2018. In vivo three-dimensional analysis of malunited forearm diaphyseal fractures with forearm rotational restriction. JBJS 100, e113.

Akhbari, B., Shah, K.N., Morton, A.M., Moore, D.C., Weiss, A.-P.C., Wolfe, S.W., Crisco, J.J., 2021. Biomechanics of the distal radioulnar joint during in vivo forearm pronosupination. J. Wrist Surg. 10, 208–215.

Ancillao, A., 2022. The helical axis of anatomical joints: calculation methods, literature review, and software implementation. Med. Biol. Eng. Comput. 60, 1815–1825.

Andreasen, C., Dahl, C., Solberg, L.B., Borgen, T.T., Wisløff, T., Gjertsen, J.-E., Figved, W., Stutzer, J.M., Nissen, F.I., Nordsletten, L., Frihagen, F., Bjørnerem, S., Omsland, T.K., 2023. Epidemiology of forearm fractures in women and men in Norway 2008–2019. Osteoporos. Int. 40, 625–633.

Baeyens, J.-P., Van Glabbeek, F., Goossens, M., Gielen, J., Van Roy, P., Clarys, J.-P., 2006. In vivo 3D arthrokinematics of the proximal and distal radioulnar joints during active pronation and supination. Clin. Biomech. S9–S12.

Blum, A., Gillet, R., Rauch, A., Urbaneja, A., Biouichi, H., Dodin, G., Germain, E., Lombard, C., Jaquet, P., Louis, M., Simon, L., Gondim Teixeira, P., 2020. 3D reconstructions, 4D imaging and postprocessing with CT in musculoskeletal disorders: past, present and future. Diagn. Interv. Imaging 101, 693–705.

Booij, R., Kämmerling, N.F., Oei, E.H.G., Persson, A., Tesselaar, E., 2023. Assessment of visibility of bone structures in the wrist using normal and half of the radiation dose with photon-counting detector CT. Eur. J. Radiol. 159, 110662.

Caruso, G., Caldari, E., Sturla, F.D., Caldaria, A., Re, D.L., Pagetti, P., Palummieri, F., Massari, L., 2021. Management of pediatric forearm fractures: what is the best therapeutic choice? A narrative review of the literature. Musculoskelet. Surg. 105, 225–234.

Choi, Y.S., Lee, Y.H., Kim, S., Cho, H.W., Song, H.-T., Suh, J.-S., 2013. Four-dimensional real-time cine images of wrist joint kinematics using dual source CT with minimal time increment scanning. Yonsei Med. J. 54, 1026–1032.

Cognet, J.-M., Mares, O., 2021. Distal radius malunion in adults. Orthop. Traumatol. Surg. Res. 107, 102755.

Colaris, J., Reijman, M., Allema, J.H., de Vries, M., Biter, U., Bloem, R., van de Ven, C., Verhaar, J., 2014. Angular malalignment as cause of limitation of forearm rotation: an analysis of prospectively collected data of both-bone forearm fractures in children. Injury 45, 955–959.

Crisco, J.J., Moore, D.C., Marai, G.E., Laidlaw, D.H., Akelman, E., Weiss, A.-P.C., Wolfe, S.W., 2007. Effects of distal radius malunion on distal radioulnar joint mechanics–an in vivo study. J. Orthop. Res. 25, 547–555.

Ehrig, R.M., Heller, M.O., 2019. On intrinsic equivalences of the finite helical axis, the instantaneous helical axis, and the SARA approach. A mathematical perspective. J. Biomech. 84, 4–10.

Garetier, M., Borotikar, B., Makki, K., Brochard, S., Rousseau, F., Ben Salem, D., 2020. Dynamic MRI for articulating joint evaluation on 1.5T and 3.0T scanners: setup, protocols, and real-time sequences. Insights Imaging 11, 66.

Iordache, S.D., Goldberg, N., Paz, L., Peylan, J., Hur, R.B., Steinmetz, A., 2017. Radiation exposure from computed tomography of the upper limbs. Acta Orthop. Belg. 83, 581–588.

Katt, B., Seigerman, D., Lutsky, K., Beredjiklian, P., 2020. Distal radius malunion. J. Hand. Surg. [Am.] 45, 433–442.

Körner, D., Gonser, C.E., Bahrs, C., Hemmann, P., 2020. Change in paediatric upper extremity fracture incidences in German hospitals from 2002 to 2017: an epidemiological study. Arch. Orthop. Trauma Surg. 140, 887–894.

Li, T.P., Wollstein, A., Sabharwal, S., Nayar, S.K., Sabharwal, S., 2022. Malunion of pediatric forearm shaft fractures: management principles and techniques. Curr. Rev. Musculoskelet. Med. 15, 427–437.

Matsuki, K.O., Matsuki, K., Mu, S., Sasho, T., Nakagawa, K., Ochiai, N., Takahashi, K., Banks, S.A., 2010. In vivo 3D kinematics of normal forearms: analysis of dynamic forearm rotation. Clin. Biomech. 25, 979–983.

Moore, D.C., Hogan, K.A., Crisco, J.J., Akelman, E., Dasilva, M.F., Weiss, A.-P.C., 2002. Three-dimensional in vivo kinematics of the distal radioulnar joint in malunited distal radius fractures. J. Hand. Surg. [Am.] 27, 233–242.

Nakamura, T., Yabe, Y., Horiuchi, Y., Yamazaki, N., 1999. In vivo motion analysis of forearm rotation utilizing magnetic resonance imaging. Clin. Biomech. 14, 315–320.

Oonk, J.G.M., Dobbe, J.G.G., Strijkers, G.J., van Rijn, S.K., Streekstra, G.J., 2023. Kinematic analysis of forearm rotation using four-dimensional computed tomography. J. Hand Surg. Eur. Vol. 48, 466–475.

Serra Lopez, V.M., Wu, C.H., Bozentka, D.J., 2023. Complications and revision surgery of forearm fractures. Hand Clin. 39, 295–306.

Shiode, R., Kabashima, M., Hiasa, Y., Oka, K., Murase, T., Sato, Y., Otake, Y., 2021. 2D–3D reconstruction of distal forearm bone from actual X-ray images of the wrist using convolutional neural networks. Sci. Rep. 11, 15249.

Shiode, R., Miyamura, S., Kazui, A., Yamamoto, N., Miyake, T., Iwahashi, T., Tanaka, H., Otake, Y., Sato, Y., Murase, T., Abe, S., Okada, S., Oka, K., 2024. Reproduction of forearm rotation dynamic using intensity-based biplane 2D–3D registration matching method. Sci. Rep. 14, 5518.

Spoor, C.W., Veldpaus, F.E., 1980. Rigid body motion calculated from spatial co-ordinates of markers. J. Biomech. 13, 391–393.

Stokdijk, M., Meskers, C.G., Veeger, H.E., de Boer, Y.A., Rozing, P.M., 1999. Determination of the optimal elbow axis for evaluation of placement of prostheses. Clin. Biomech. (Bristol, Avon) 14, 177–184.

Tay, S.C., van Riet, R., Kazunari, T., Amrami, K.K., An, K.-N., Berger, R.A., 2010. In-vivo kinematic analysis of forearm rotation using helical axis analysis. Clin. Biomech. 25, 655–659.

Truntzer, J., Vopat, M.L., Kane, P.M., Christino, M.A., Katarincic, J., Vopat, B.G., 2015. Forearm diaphyseal fractures in the adolescent population: treatment and management. Eur. J. Orthop. Surg. Traumatol. 25, 201–209.

van Loon, D.F.R., van Es, E.M., Eygendaal, D., Veeger, D.H.E.J., Colaris, J.W., 2024. Automatic identification of radius and ulna bone landmarks on 3D virtual models. Comput. Biol. Med. 179, 108891.

Veeger, H.E., Yu, B., An, K.N., Rozendal, R.H., 1997. Parameters for modeling the upper extremity. J. Biomech. 30, 647–652.

Woltring, H.J., 1990. Estimation of the trajectory of the instantaneous centre of rotation in planar biokinematics. J. Biomech. 23, 1273–1274.

Wu, G., van der Helm, F.C.T., Veeger, H.E.J. DirkJan, Makhsous, M., Van Roy, P., Anglin, C., Nagels, J., Karduna, A.R., McQuade, K., Wang, X., Werner, F.W., Buchholz, B., 2005. ISB recommendation on definitions of joint coordinate systems of various joints for the reporting of human joint motion—part II: shoulder, elbow, wrist and hand. J. Biomech. 38, 981–992.

Youm, Y., Dryer, R.F., Thambyrajah, K., Flatt, A.E., Sprague, B.L., 1979. Biomechanical analyses of forearm pronation-supination and elbow flexion-extension. J. Biomech. 12, 245–255.